Journal of Materials Chemistry A

COMMUNICATION

View Article Online
View Journal | View Issue

Cite this: J. Mater. Chem. A, 2018, 6, 6220

Received 20th February 2018
Accepted 16th March 2018

DOI: 10.1039/c8ta01695j

rsc.li/materials-a

Facile template-free synthesis of uniform carbon-confined V_2O_3 hollow spheres for stable and fast lithium storage†

Chunhua Han,* Fang Liu, Jinshuai Liu, Qi Li, Jiashen Meng, Bowen Shao, Qiu He, Xuanpeng Wang, Ziang Liu and Liqiang Mai*

A facile template-free method has been successfully developed to synthesize uniform nitrogen-doped carbon-confined V_2O_3 hollow spheres by a mismatched coordination reaction, an inside-out Ostwald-ripening solvothermal process and subsequent heat treatment. Notably, the delicate composite as an anode material displayed superior rate capability and excellent cycling stability for lithium-ion batteries.

Nowadays, clean energy is highly desired to alleviate the energy shortage and environmental pollution because of the impending exhaustion and serious lack of fossil fuels.[1,2] The lithium-ion battery (LIB) as one important representative of secondary energy storage devices has drawn widespread attention on account of its combination of relatively high energy density, long lifespan and environmental benignity.[3–6] To meet the growing energy demands, more efficient LIBs which have high rate, high specific capacity and long-term cycling stability are greatly essential.[7–10] However, graphite, the most common anode material in commercial LIBs, has a limited theoretical specific capacity of 372 mA h g^{-1}, which hardly meets the requirements of future energy-storage systems. Transition metal oxides as alternatives to graphite have attracted considerable attention in the past decade due to their abundant resources, low cost and high theoretical capacities (>700 mA h g^{-1}).[11] However, the huge volume change during the lithium insertion/extraction process and poor electrical conductivity limit their practical application.

Intensive efforts have been dedicated to developing various methods to improve the electrochemical performance of metal oxides for LIBs.[12–15] One typical strategy is to fabricate metal oxide hollow structures with high uniformity and abundant interiors, which can shorten the ion/electron transport distance and accommodate large volume variations.[16–21] For instance, various metal oxide hollow structures with enhanced lithium storage have been successfully synthesized, including SnO_2 hollow spheres, multi-shelled Fe_3O_4 microboxes, multi-shelled V_2O_5 microspheres, double-shelled $CoMn_2O_4$ hollow microcubes, *etc.*[22–25] A common synthetic method for hollow structures is hard template-assisted synthesis, involving the preparation of templates, the templating treatment and the removal of templates. However, this template-assisted method is usually complex, time consuming and involves a relatively high cost. Therefore, a facile template-free synthesis strategy for the scalable fabrication of uniform hollow structures is highly desired. To improve the electron conductivity and structural stability of metal oxides, another efficient method is integrating them with various carbon materials to generate well-connected composites.[26,27] For example, Wang *et al.* synthesized gelatin-derived Fe_3O_4/carbon hybrids, which exhibited superior rate capability and good cycling performance for LIBs. Recently, Meng *et al.* reported carbon-confined SnO_2 nanodots anchored on graphene with ultrafast and stable lithium storage.[28] In addition, the intrinsic electron conductivity of metal oxides plays an important role in its rate performance. Different from other semiconducting metal oxides, the rhombohedral corundum-type V_2O_3 displays metallic behavior because the electrons in the V-3d orbital can travel along the V–V chains.[29,30] This phenomenon can also be verified by theoretical calculations, indicating that V_2O_3 is one ideal candidate of LIB anode materials. However, to combine the above-mentioned merits and improve the lithium storage performance, controlled synthesis of uniform carbon-confined V_2O_3 hollow structures by a simple synthesis strategy still remains a great challenge.

Herein, we develop a facile and efficient template-free synthesis of uniform nitrogen-doped carbon-confined V_2O_3 hollow spheres through a two-step process. First, a mismatched coordination reaction between vanadium ions and organic ligands occurs during the solvothermal process, resulting in the

State Key Laboratory of Advanced Technology for Materials Synthesis and Processing, International School of Materials Science and Engineering, Wuhan University of Technology, Luoshi Road 122, Wuhan, Hubei, 430070, China. E-mail: hch5927@whut.edu.cn; mlq518@whut.edu.cn

† Electronic supplementary information (ESI) available: X-ray diffraction, cyclic voltammetry, thermogravimetric analysis, morphological characterization, and electrochemical impedance spectroscopy. See DOI: 10.1039/c8ta01695j

formation of an amorphous organic–inorganic complex precursor. On prolonging the solvothermal time, the precursor morphology evolves from solid microspheres to yolk–shell microspheres and eventually hollow microspheres due to an inside-out Ostwald-ripening. Then, after *in situ* carbonization, the as-prepared precursor hollow spheres are converted into uniform morphology-preserved nitrogen-doped carbon-confined V_2O_3 (denoted as V_2O_3@NC) hollow spheres. The delicate architecture can provide high activity, high electron conductivity, short diffusion length, robust structure and good strain accommodation, which are beneficial for LIBs (Fig. S1, ESI†). As a proof-of-concept application, when evaluated as a LIB anode material, the resulting V_2O_3@NC hollow spheres exhibit high capacity, excellent rate capability and long-term cycling stability.

The formation mechanism of uniform V_2O_3@NC hollow spheres is shown in Fig. 1. First, vanadium(III) acetylacetonate (denoted as V(acac)) and 2-dimethylimidazole (2-MIM) were selected as the metal source and organic ligand, respectively, and were both dissolved in *N*,*N*-dimethylformamide (DMF), forming a homogeneous solution. Then, during the solvothermal process, due to the mismatched bonding angles and/or distorted polyhedra, a mismatched coordination reaction occurred between V(acac) and 2-MIM, resulting in the formation of amorphous metal–ligand (V–2-MIM) complexes.[31,32] This above-mentioned reaction was also revealed to distinguish that of metal–organic frameworks (MOFs) in our previous work.[28] During the initial stage (step I), V–2-MIM complex solid spheres were firstly obtained after reaction for 3 h due to fast nucleation and growth rates. The scanning electron microscopy (SEM) image and transmission electron microscopy (TEM) image showed uniform solid spheres with smooth surfaces and a diameter of about 150 nm (Fig. 2a and d). When the reaction time was extended to 6 h (step II), the morphology of the V–2-MIM complexes transformed from solid spheres to yolk–shell spheres, which was demonstrated by SEM and TEM images (Fig. 2b and e and S2, ESI†). This transformation was attributed to an inside-out Ostwald-ripening process, which involved the consumption of the interior cores in solid spheres and the recrystallization on sphere shells.[33] With a further increase of reaction time up to 12 h (step III), uniform V–2-MIM complex hollow spheres with rough surfaces were eventually obtained (Fig. 2c and f and S3, ESI†). This whole structural evolution was driven by the reduction of Gibbs free energy in the reaction system.[34] The selected area electron diffraction (SAED) patterns and X-ray diffraction (XRD) patterns of these V–2-MIM complexes indicated an amorphous nature (inset of Fig. 2d–f and g–i), which was attributed to the above-mentioned mismatched coordination reaction. Finally, after *in situ* carbonization in argon (step IV), the morphology-preserved V_2O_3@NC hollow spheres were successfully obtained. In brief, the facile and efficient template-free synthesis strategy, which involves a mismatched coordination reaction, an inside-out Ostwald-ripening solvothermal process and subsequent heat treatment, shows great potential for further practical application.

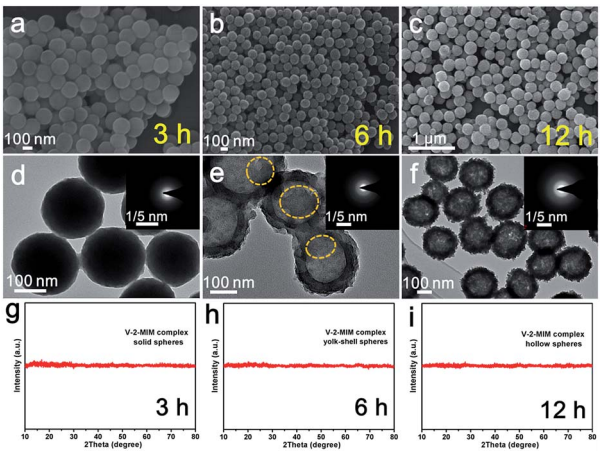

Fig. 2 Characterization of the structural evolution of the V–2-MIM precursors prepared at different times during the solvothermal process. SEM images (a–c), TEM images (d–f) and XRD patterns (g–i) of the samples prepared at 3, 6 and 12 h, respectively. Insets of (d–f) are the corresponding SAED patterns. The yellow dotted circles mark the cores.

The preparation of uniform and high-quality amorphous V–2-MIM complex hollow spheres is crucial to the formation of V_2O_3@NC hollow spheres during the fabrication process. To further reveal the structure of the V–2-MIM complex hollow spheres after solvothermal reaction, a series of characterization experiments were carried out (Fig. 3). The SEM images showed that the obtained V–2-MIM complex hollow spheres were uniform with an average size of ~200 nm in diameter and rough surfaces (Fig. 3a–c). According to a statistical analysis, the diameters of these hollow spheres exhibited regular distribution, further confirming their uniformity (Fig. S4, ESI†). Some

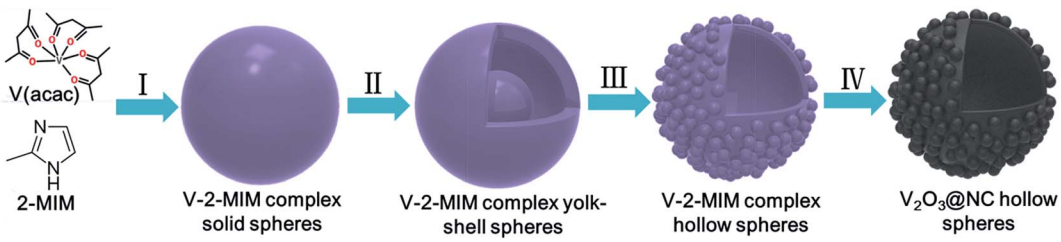

Fig. 1 Schematic illustration of the formation process of uniform V_2O_3@NC hollow spheres. (I–III) Time-dependent structural evolution of the V–2-MIM complex spheres during the solvothermal process. (IV) Heat treatment in an argon atmosphere.

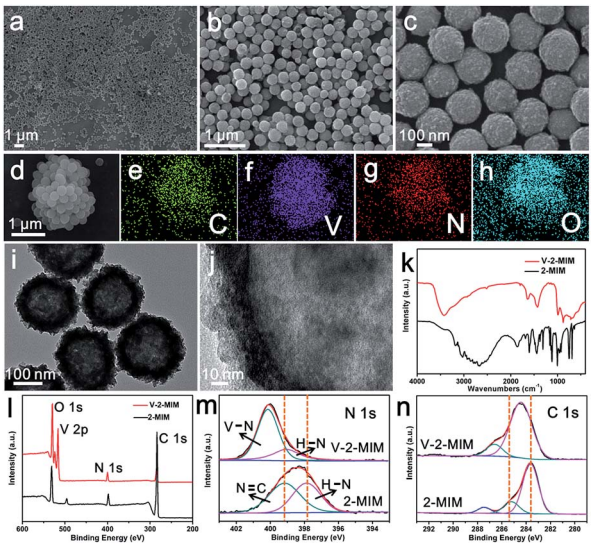

Fig. 3 (a–c) SEM images of the V–2-MIM complex hollow spheres. (d–h) SEM image and the corresponding EDX mapping images of the V–2-MIM complex hollow spheres. (i and j) TEM images of the V–2-MIM complex hollow spheres. (k–n) FTIR, XPS, and high-resolution N 1s and C 1s XPS spectra of the V–2-MIM complex hollow spheres and 2-MIM raw material, respectively.

broken hollow spheres demonstrated interior hollow voids. The energy-dispersive X-ray (EDX) elemental mapping images displayed the uniform distribution of V, C, N and O (Fig. 3d–h). The TEM images revealed that the shells of the V–2-MIM complex hollow spheres had a uniform thickness of ~30 nm and rough surfaces, which were composed of small nanoparticles due to the Ostwald-ripening process (Fig. 3i and j). The nitrogen adsorption–desorption isotherms of the V–2-MIM complex hollow spheres displayed a Brunauer–Emmett–Teller (BET) specific surface area of 39.3 $m^2\ g^{-1}$, much lower than that of crystalline MOFs (generally >500 $m^2\ g^{-1}$) (Fig. S5, ESI†). The pore size distribution was from 3 to 7 nm, corresponding to typical mesopores. This distribution was mainly attributed to the random and loose stacking of nanoparticles, which was consistent with the above TEM observation.

Furthermore, thermogravimetric-differential scanning calorimetry (TG-DSC) measurements were carried out to investigate the pyrolysis process of the V–2-MIM complex hollow spheres (Fig. S6, ESI†). The pyrolysis process in argon involved two stages of mass loss including solvent volatilization (<250 °C) and carbonization of the bonding organic ligands in the V–2-MIM complex (300–500 °C). However, in an air atmosphere, the mass first decreased and then increased, which was attributed to the oxidation of low-valence vanadium(III). On the basis of Fourier-Transform Infrared (FTIR) analysis, the complex hollow spheres exhibited the typical vibrations of 2-MIM along with peak shifts, indicating the occurrence of a mismatched coordination reaction. X-ray photoelectron spectroscopy (XPS) was carried out to reveal the bonds formed in the obtained complex hollow spheres. The XPS full spectrum indicated that the typical peaks of C, N, O and V elements existed in the product (Fig. 3l). The XPS spectrum of 2-MIM was also measured for comparison (Fig. 3). In the high-resolution N 1s XPS spectrum of 2-MIM, the two typical peaks located at 397.8 and 399.2 eV corresponded to the H–N bond and N=C bond. Their similar peak areas indicated that the atomic ratio was 1, which was consistent with the molecular structure of 2-MIM. The high-resolution N 1s XPS spectrum of the V–2-MIM complex precursor showed the formation of a new V–N bond and a positive shift of characteristic bond energies, indicating that the V ions could directly bond with the N atoms of 2-MIM by coordination reaction. This positive shift phenomenon was due to the electron transfer from N atoms to V ions in V–2-MIM. However, the remaining H–N bonds were attributed to the incomplete coordination reaction. In addition, position shifts of typical peaks were also observed in the high-resolution C 1s XPS spectrum of the V–2-MIM complex precursor. The mass concentration of V in the amorphous V–2-MIM complex hollow spheres determined by XPS was 38.5 wt%, which is close to that from inductively coupled plasma atomic emission spectroscopy (ICP-AES) (40.2 wt%) (Fig. S7, ESI†). Therefore, the mismatched coordination reaction between V ions and 2-MIM plays an important role in the formation of uniform amorphous complex hollow spheres.

Uniform V_2O_3@NC hollow spheres were easily obtained after *in situ* carbonization of the as-prepared V–2-MIM complex hollow spheres. A series of characterization experiments were carried out. As shown in Fig. 4a, the XRD pattern of the obtained product can be well indexed to the rhombohedral corundum-type V_2O_3 phase (JCPDS card no. 00-034-0187) without any impurity. Low-magnification SEM images showed remarkably uniform spheres from all selected views (Fig. 4b and S8a, ESI†). The high-magnification SEM image demonstrated that the obtained spheres had an average diameter of ~200 nm and rough surfaces, which were composed of many tiny nanoparticles (Fig. 4c). Some broken spheres suggested hollow inner voids with thin shells. TEM images further confirmed uniform hollow spheres and thin shells about 30 nm in thickness (Fig. 4d and e and S8b and c, ESI†). High-resolution TEM (HRTEM) images

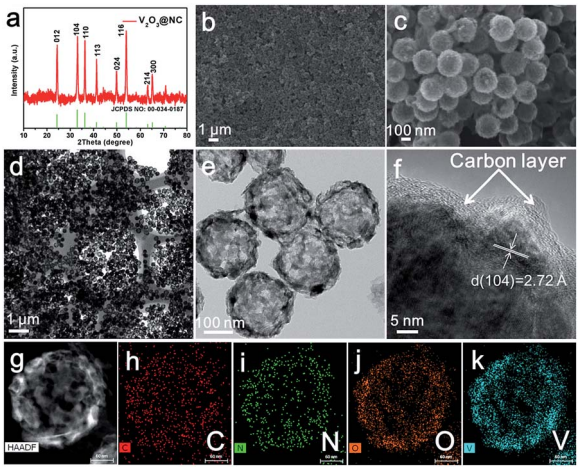

Fig. 4 Characterization of the uniform V_2O_3@NC hollow spheres. (a) XRD pattern. (b and c) SEM images. (d and e) TEM images. (f) HRTEM image. (g–k) STEM image and the corresponding STEM-EDS mapping images.

revealed a thin continuous carbon layer ~2 nm in thickness uniformly confined onto the external V_2O_3 nanocrystals (Fig. 4f and S8d, ESI†). A lattice fringe with an interlayer spacing of 2.72 Å can be clearly observed and is well indexed to the (104) lattice plane of V_2O_3. Scanning-TEM high-angle annular dark-field (STEM-HAADF) measurements were also carried out to demonstrate the obtained hollow spheres (Fig. 4g). As shown in Fig. 4h–k, the STEM-energy-dispersive spectroscopy (STEM-EDS) mapping images confirmed the uniform distribution of C, N, O and V, and were completely consistent with the selected image. The nitrogen adsorption–desorption isotherm of the V_2O_3@NC hollow spheres displayed a high BET specific surface area of 21.7 $m^2\ g^{-1}$, which could increase the electrode/electrolyte contact area and facilitate Li^+ transport (Fig. S9a and b, ESI†). Raman spectroscopy was conducted to characterize the nature of carbon in the V_2O_3@NC hollow spheres (Fig. S9c, ESI†). The typical signatures located at about 1350 and 1600 cm^{-1} were attributed to the D and G bands, respectively, indicating its partial graphitization. On the basis of TG-DSC analysis, the mass content of carbon was calculated to be about 8 wt% (Fig. S9, ESI†).

To further reveal their superiority, the as-prepared V_2O_3@NC hollow spheres were utilized as an anode material for LIBs. First, the cyclic voltammetry (CV) curves of the first four cycles were measured at a scan rate of 0.2 mV s^{-1} within the voltage window of 0.01–3 V *vs.* Li^+/Li (Fig. 5a). During the first discharge process, a clear peak located at around 0.7 V was observed, which could be mainly attributed to the formation of a solid electrolyte interphase (SEI) layer. The three subsequent CV curves mostly overlapped, showing highly reversible lithium storage. When tested at a current density of 200 mA g^{-1}, the V_2O_3@NC hollow spheres exhibited a first discharge capacity of 915 mA h g^{-1} and a first charge capacity of 735 mA h g^{-1}, corresponding to a high initial coulombic efficiency of 80.3% (Fig. 5b). After 120 cycles, the electrode still retained a high reversible discharge capacity of 811 mA h g^{-1} and an outstanding capacity retention of over 100%. Furthermore, the V_2O_3@NC hollow spheres were tested at various current densities ranging from 100 to 5000 mA g^{-1} to evaluate the rate capability (Fig. 5c). The obtained electrode delivered average discharge capacities of 785, 701, 599, 528, 458 and 361 mA h g^{-1} at different current densities of 100, 200, 500, 1000, 2000 and 5000 mA g^{-1}, respectively. When returned to 100 mA g^{-1}, the discharge capacity of the V_2O_3@NC hollow spheres can recover to 845 mA h g^{-1} and increase to 981 mA h g^{-1} after 100 cycles. The corresponding charge–discharge voltage profiles of rate performance are shown in Fig. 5d, indicating low polarization and high reversibility. Furthermore, the long-term cycling performance of the V_2O_3@NC hollow spheres at 2000 mA g^{-1} was investigated (Fig. 5e). After 700 cycles, a high specific capacity of 472 mA h g^{-1} and a high capacity retention of over 100% were obtained, showing excellent long-term cycling stability. Notably, the increased capacity of the V_2O_3@NC hollow spheres may be attributed to the formation of an electrochemical gel-like polymer layer and the size reduction of the vanadium oxide nanocrystals, which is also widely observed for many transition metal oxides. In addition, compared with other carbon-based V_2O_3 nanostructures in previous studies, our synthesized V_2O_3@NC hollow spheres displayed fast and stable lithium storage (Table S1, ESI†).[35–41]

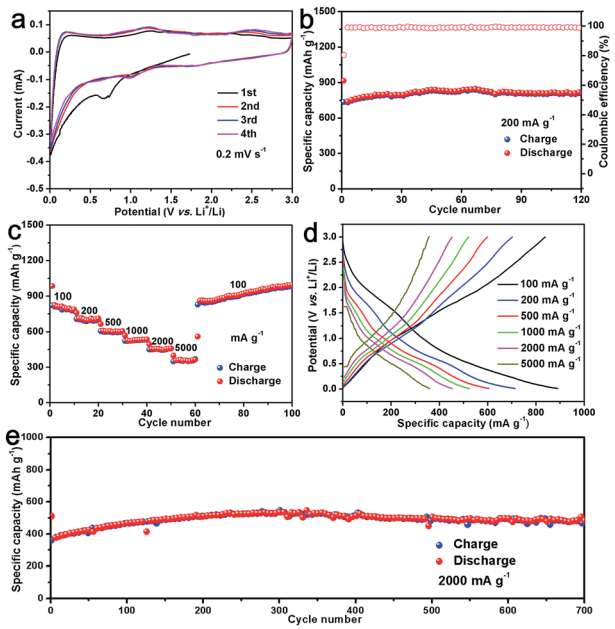

Fig. 5 Lithium storage performance of the uniform V_2O_3@NC hollow spheres. (a) The first four CV curves at a scan rate of 0.2 mV s^{-1}. (b) Cycling performance at a low current density of 200 mA g^{-1}. (c) Rate performance at different current densities ranging from 100 to 200, 500, 1000, 2000, and 5000, and back to 100 mA g^{-1}. (d) The corresponding charge–discharge curves at different current densities. (e) Long-term cycling performance at a high current density of 2000 mA g^{-1}.

The superior lithium storage performance of the V_2O_3@NC hollow spheres can be attributed to their unique architecture that provides short ion diffusion length, high conductivity, robust structure and good strain accommodation. A series of characterization experiments were carried out to reveal the structure–performance relationships. First, electrochemical impedance spectroscopy (EIS) was conducted to evaluate the charge-transfer resistance (R_{ct}) of the V_2O_3@NC hollow spheres (Fig. S10b, ESI†). A small R_{ct} value of 118 Ω after 10 cycles indicated fast interface electron mobility. Furthermore, the lithium storage kinetic analysis displays obvious lithiation pseudo-capacitive behavior (Fig. S11, ESI†). Based on the quantification, 79.5% of the total capacity is capacitive at a scan rate of 4 mV s^{-1}. In addition, the morphology of the V_2O_3@NC hollow spheres can be well maintained after 50 cycles at 200 mA g^{-1} (Fig. S12, ESI†).

Conclusions

In summary, we have developed a facile template-free synthesis of uniform V_2O_3@NC hollow spheres *via* solvothermal reaction and successive annealing treatments. On the basis of experimental analysis, the formation mechanism was clearly revealed. The resulting architecture can provide high surface area, short ion diffusion length, high electronic conductivity, robust structure and good strain accommodation. When employed as an

anode material, the resulting V_2O_3@NC hollow spheres show excellent rate capability and remarkable cycling stability for LIBs. Specifically, even at 2 A g^{-1} after 700 cycles, the electrode displayed a high reversible capacity of 472 mA h g^{-1} with a capacity retention of over 100%. Therefore, our work presents a facile and efficient strategy for the delicate synthesis of unique carbon-based nanostructures for potential energy-related applications.

Conflicts of interest

There are no conflicts to declare.

Acknowledgements

This work was supported by the National Natural Science Fund for Distinguished Young Scholars (51425204), the National Natural Science Foundation of China (51521001 and 51302203), the National Key Research and Development Program of China (2016YFA0202603), the Programme of Introducing Talents of Discipline to Universities (B17034), the Yellow Crane Talent (Science & Technology) Program of Wuhan City, and the Fundamental Research Funds for the Central Universities (WUT: 2016III001 and 2017III040).

References

1 S. Chu, Y. Cui and N. Liu, *Nat. Mater.*, 2016, **16**, 16–22.
2 C. P. Grey and J. M. Tarascon, *Nat. Mater.*, 2016, **16**, 45–56.
3 J. Lu, Z. Chen, Z. Ma, F. Pan, L. A. Curtiss and K. Amine, *Nat. Nanotechnol.*, 2016, **11**, 1031–1038.
4 Z. Yang, J. Zhang, M. C. Kintner-Meyer, X. Lu, D. Choi, J. P. Lemmon and J. Liu, *Chem. Rev.*, 2011, **111**, 3577–3613.
5 L. Mai, M. Yan and Y. Zhao, *Nature*, 2017, **546**, 469–470.
6 Z. Xiao, J. Meng, Q. Li, X. Wang, M. Huang, Z. Liu, C. Han and L. Mai, *Sci. Bull.*, 2018, **63**, 46–53.
7 Y. Tang, Y. Zhang, W. Li, B. Ma and X. Chen, *Chem. Soc. Rev.*, 2015, **44**, 5926–5940.
8 A. Manthiram, *ACS Cent. Sci.*, 2017, **3**, 1063–1069.
9 C. Wang, Z. Guo, W. Shen, Q. Xu, H. Liu and Y. Wang, *Adv. Funct. Mater.*, 2014, **24**, 5511–5521.
10 Y. Xu, W. Shen, A. Zhang, H. Liu and Z. Ma, *J. Mater. Chem. A*, 2014, **2**, 12982–12990.
11 Y. Zhong, M. Yang, X. Zhou and Z. Zhou, *Mater. Horiz.*, 2015, **2**, 553–566.
12 Y. Zhao, L. P. Wang, M. T. Sougrati, Z. Feng, Y. Leconte, A. Fisher, M. Srinivasan and Z. Xu, *Adv. Energy Mater.*, 2017, **7**, 1601424.
13 Y. Liu, G. Zhou, K. Liu and Y. Cui, *Acc. Chem. Res.*, 2017, **50**, 2895–2905.
14 J. Meng, H. Guo, C. Niu, Y. Zhao, L. Xu, Q. Li and L. Mai, *Joule*, 2017, **1**, 522–547.
15 C. Yuan, H. B. Wu, Y. Xie and X. W. Lou, *Angew. Chem., Int. Ed.*, 2014, **53**, 1488–1504.
16 Y. Zhao and L. Jiang, *Adv. Mater.*, 2009, **21**, 3621–3638.
17 J. Meng, C. Niu, L. Xu, J. Li, X. Liu, X. Wang, Y. Wu, X. Xu, W. Chen, Q. Li, Z. Zhu, D. Zhao and L. Mai, *J. Am. Chem. Soc.*, 2017, **139**, 8212–8221.
18 L. Zhou, Z. Zhuang, H. Zhao, M. Lin, D. Zhao and L. Mai, *Adv. Mater.*, 2017, **29**, 1602914.
19 K. X. Wang, X. H. Li and J. S. Chen, *Adv. Mater.*, 2015, **27**, 527–545.
20 C. Niu, J. Meng, X. Wang, C. Han, M. Yan, K. Zhao, X. Xu, W. Ren, Y. Zhao, L. Xu, Q. Zhang, D. Zhao and L. Mai, *Nat. Commun.*, 2015, **6**, 7402.
21 C. Yuan, J. Li, L. Hou, L. Zhang and X. Zhang, *Part. Part. Syst. Charact.*, 2014, **31**, 657–663.
22 X. W. Lou, C. M. Li and L. A. Archer, *Adv. Mater.*, 2009, **21**, 2536–2539.
23 L. Zhang, H. B. Wu and X. W. Lou, *J. Am. Chem. Soc.*, 2013, **135**, 10664–10672.
24 L. Zhou, D. Zhao and X. W. Lou, *Adv. Mater.*, 2012, **24**, 745–748.
25 J. Wang, H. Tang, L. Zhang, H. Ren, R. Yu, Q. Jin, J. Qi, D. Mao, M. Yang, Y. Wang, P. Liu, Y. Zhang, Y. Wen, L. Gu, G. Ma, Z. Su, Z. Tang, H. Zhao and D. Wang, *Nat. Energy*, 2016, **1**, 16050.
26 R. Liu, J. Duay and S. B. Lee, *Chem. Commun.*, 2011, **47**, 1384–1404.
27 J. Meng, X. Liu, J. Li, Q. Li, C. Zhao, L. Xu, X. Wang, F. Liu, W. Yang, X. Xu, Z. Liu, C. Niu and L. Mai, *Nano Lett.*, 2017, **17**, 7773–7781.
28 J. Meng, Z. Liu, C. Niu, L. Xu, X. Wang, Q. Li, X. Wei, W. Yang, L. Huang and L. Mai, *Mater. Horiz.*, 2018, **5**, 78–85.
29 Y. Sun, S. Jiang, W. Bi, C. Wu and Y. Xie, *J. Power Sources*, 2011, **196**, 8644–8650.
30 Y. Cai, G. Fang, J. Zhou, S. Liu, Z. Luo, A. Pan, G. Cao and S. Liang, *Nano Res.*, 2017, **11**, 449–463.
31 H. Ejima, J. J. Richardson, K. Liang, J. P. Best, M. P. van Koeverden, G. K. Such, J. Cui and F. Caruso, *Science*, 2013, **341**, 154–157.
32 J. Guo, Y. Ping, H. Ejima, K. Alt, M. Meissner, J. J. Richardson, Y. Yan, K. Peter, D. von Elverfeldt, C. E. Hagemeyer and F. Caruso, *Angew. Chem., Int. Ed.*, 2014, **53**, 5546–5551.
33 A. Pan, H. B. Wu, L. Yu and X. W. D. Lou, *Angew. Chem., Int. Ed.*, 2013, **125**, 2282–2286.
34 W. Shi, S. Song and H. Zhang, *Chem. Soc. Rev.*, 2013, **42**, 5714–5743.
35 X. An, H. Yang, Y. Wang, Y. Tang, S. Liang, A. Pan and G. Cao, *Sci. China Mater.*, 2017, **60**, 717–727.
36 S. Gao, D. Zhang, K. Zhu, J. A. Tang, Z. Gao, Y. Wei, G. Chen and Y. Gao, *J. Alloys Compd.*, 2017, **702**, 13–19.
37 L. Jiang, Y. Qu, Z. Ren, P. Yu, D. Zhao, W. Zhou, L. Wang and H. Fu, *ACS Appl. Mater. Interfaces*, 2015, **7**, 1595–1601.
38 C. Niu, M. Huang, P. Wang, J. Meng, X. Liu, X. Wang, K. Zhao, Y. Yu, Y. Wu, C. Lin and L. Mai, *Nano Res.*, 2015, **9**, 128–138.
39 Y. Wang, H. J. Zhang, A. S. Admar, J. Luo, C. C. Wong, A. Borgna and J. Lin, *RSC Adv.*, 2012, **2**, 5748–5753.
40 L. Zeng, C. Zheng, J. Xi, H. Fei and M. Wei, *Carbon*, 2013, **62**, 382–388.
41 Y. Zhang, A. Pan, S. Liang, T. Chen, Y. Tang and X. Tan, *Mater. Lett.*, 2014, **137**, 174–177.

